JOURNAL OF THERMOPHYSICS AND HEAT TRANSFER
Vol. 8, No. 4, Oct.–Dec. 1994

Two-Temperature Modeling of Laser Sustained Hydrogen Plasmas

Ayhan E. Mertogul* and Herman Krier†
University of Illinois at Urbana-Champaign, Urbana, Illinois 61801

A kinetic nonequilibrium model of laser sustained hydrogen plasmas has been formulated and solved for the prediction of steady-state energy transport processes. This model is the first of its kind and includes a discretized beam ray-trace with a variable index of refraction based upon plasma electron number density for a 10.6-μm CO_2 laser input. Model results for fraction of incident laser power absorbed, and fraction of incident laser power retained by the hydrogen gas have compared favorably with experimental results. The model has been used to provide predictions of laser sustained plasma (LSP) performance well outside the realm of experiments to incident powers as high as 700 kW. At the gas pressures studied, minimal kinetic nonequilibrium was observed in LSP core regions, even for 700-kW laser power.

Introduction

LASER rocket propulsion is a concept wherein propellant is heated through the absorption of a remotely based laser beam. The remote beam is focused into an absorption chamber, where it is absorbed by the propellant gas. The vehicle by which laser energy is absorbed is the laser sustained plasma (LSP). The primary mechanism for laser absorption in the LSP is inverse bremsstrahlung (IB) in which a photon is absorbed by an electron in the presence of a third particle that carries off excess momentum. Without some initial source of electrons the beam would not be absorbed and would pass through the propellant unattenuated. However, once initiated, and assuming that the absorption chamber conditions are within LSP stability limits, the LSP will stabilize at a position in the propellant flow and the focused beam where a balance exists between power absorbed from the beam and power lost to the propellant and surroundings through conduction, convection, and radiation. Unfortunately, this power balance cannot always be maintained, and the plasma may not always be stable. Assuming the LSP is stable, there are two global quantities that are used to describe its performance. Global absorption is defined as the fraction of incident laser power absorbed by the electrons in the LSP through inverse bremsstrahlung. Thermal efficiency is defined as the fraction of incident laser power retained by the propellant as thermal energy.

The transfer of energy from electrons to the heavy species is mainly due to collisions. However, due to the great disparity between the masses of electrons and the heavy species, energy transfer between these particles is inefficient when compared to collisional energy transfer between particles of similar mass. It is therefore possible that a combination of high beam absorption and low collisional relaxation could cause the electrons and the heavy species to each have a distinct kinetic temperature.

There are five control parameters that may be varied to alter the LSP condition. These parameters are 1) the incident laser power, 2) the incident propellant mole flux, 3) the chamber ambient gas pressure, 4) the beam focusing geometry, and 5) the beam wavelength. The LSP will always stabilize with the plasma front upstream of the laser focus. If, due to some perturbation, the power flux is insufficient to maintain the LSP power balance, then the LSP will restabilize closer to the beam focus where the power flux is higher. If the power flux at the focus is insufficient to maintain the LSP power balance, then the LSP will continue through to the downstream side of the focus where no position in the beam has sufficient power flux to stabilize it. The net effect is that the plasma extinguishes, and the phenomenon is commonly referred to as blowout. A more detailed discussion of LSP stability may be found in Refs. 1–3.

There have been very few experimental studies involving laser sustained hydrogen plasmas. Here the distinction between a pulsed plasma and a steady-state plasma should be made. Pulsed plasmas are produced using a high-power, short duration pulsed laser. Pulsed plasmas have been produced in hydrogen to study breakdown intensity[4–6] as well as electron recombination rate.[7] Kozlov et al.[8] studied the effect of pressure and power variations on steady-state hydrogen plasma stability using a 1-kW continuous wave CO_2 laser at pressures from 1 to 10 atm. Mertogul et al.[3] presented the first quantitative study of hydrogen LSPs, including measurements of global absorption, thermal efficiency, and stability limits.[3]

Global measurements are useful in providing information regarding the effects of the control parameters on overall system performance, but not on the detailed structure of the LSP and the actual energy transfer mechanisms. The goal of this work was to develop a model for the prediction of global absorption and thermal efficiency at very high input laser powers as would be used in an actual thruster.

Review of LSP Models

All previous models of LSPs, regardless of the type of propellant considered, the method of calculating energy absorbed, or the numerical solution scheme have assumed local thermodynamic equilibrium (LTE) to be a valid assumption. A summary of modeling efforts can be seen in Table 1.

The most recent LSP model was that of Eguiguren and Krier,[19] which was similar in many ways to the earlier model of Jeng and Keefer.[15] A useful aspect of the results of Refs. 15 and 19 were the predictions of global absorption and thermal efficiency, as well as temperature and stream function contours for argon and hydrogen.

Predicted results for global absorption and thermal efficiency for argon from the Eguiguren and Krier model only

Presented as Paper 93-3224 at the AIAA 24th Plasmadynamics and Lasers Conference, Orlando, FL, July 6–9, 1993; received Oct. 8, 1993; revision received April 5, 1994; accepted for publication April 29, 1994. Copyright © 1993 by the American Institute of Aeronautics and Astronautics, Inc. All rights reserved.

*Postdoctoral Research Associate, Department of Mechanical and Industrial Engineering, 1206 W. Green Street, Rm. 140. Member AIAA.

†Professor, Department of Mechanical and Industrial Engineering, 1206 W. Green Street, Rm. 140. Fellow AIAA.

Table 1 Summary of LSP modeling efforts

Year	Reference	Comments/features
1970	9	One-dimensional, air at 1 atm, radiation loss
1979	10	One-dimensional, hydrogen from 1 to 30 atm, radiation loss
1982	11	Quasi-two-dimensional, argon
1984	12	Two-dimensional, hydrogen, "focused" beam, cons. abs. coeff.
1985	13	Two-dimensional, hydrogen, ray-trace, seeding
1986	14	Quasi-two-dimensional, argon, "focused beam"
1987	15	Two-dimensional, hydrogen, ray-trace
1987	16	Two-dimensional, hydrogen, ray-trace, thruster
1987	17	Two-dimensional, argon, no rays
1987	18	Two-dimensional, argon and hydrogen, no rays
1989	19	Two-dimensional, argon and hydrogen at 1 atm

partially agreed with experimental data. Both experimental data and model predictions indicated that thermal efficiency increased with mole flux. However, at a fixed mole flux, model predictions for thermal efficiency were well in excess of experimental data.[19]

The errors associated with the predicted values of thermal efficiency may have been due to the assumption of LTE. This assumption has since been proven to be incorrect by Zerkle,[20] whose experiments demonstrated electron temperatures elevated well above gas temperatures for argon LSPs. Hotter non-LTE electrons would radiate more than would be predicted by an LTE model, thereby causing an overprediction for thermal efficiency.

Although significant work has been done on LSP modeling, none of the models were considered to be adequate for the purpose of predicting very high-power LSPs because of two important missing features. First, all the previous LSP models assumed LTE to be valid. However, preferential heating of the electrons by a high-intensity laser beam casts doubt on this assumption. Furthermore, LTE has been experimentally shown not to be valid for argon LSPs at 1 atm by Zerkle.[20]

The second important missing feature was that of a physical beam ray-trace including a variable refractive index within the solution domain. Although some of the previous models were described as having some form of beam ray-trace, none of them included the effects of a change in refractive index.

Kinetic Nonequilibrium Model

Originally, the non-LTE computational model was formulated with as few assumptions regarding the thermodynamic state as possible. Model assumptions included laminar and axisymmetric flow, and steady-state conditions. With regard to thermodynamic state, all heavy species were assumed to share a common heavy kinetic temperature T_g. Radiation was discretized into a number of discrete bands and lines for use in a collisional-radiative rate model.[1]

As a limiting case, the original non-LTE model was simplified. Since the physical processes in an LSP are linked, care was taken in what was neglected and what was retained to insure that the simplified model had a physical basis. The first assumption of the simplified model was that kinetic nonequilibrium is possible. Therefore, the simplified model retained two kinetic temperatures and two energy equations.

Chemical equilibrium was assumed, and only the major hydrogen plasma species [e^-, H^+, H(n), H_2] number densities were computed using an iterative algorithm.[1] The simplified model retains only the continuum radiation of the electrons, which was assumed to be optically thin.

The conservation equations for the kinetic nonequilibrium model are now presented. The electron energy equation is

$$\frac{\partial}{\partial x}\left[\left(\frac{3}{2}k_b n_e u\right)T_e\right] + \frac{1}{r}\frac{\partial}{\partial r}\left[\left(\frac{3}{2}rk_b n_e v\right)T_e\right] = \frac{\partial}{\partial x}\left(\lambda_e \frac{\partial T_e}{\partial x}\right) + \frac{1}{r}\frac{\partial}{\partial r}\left(r\lambda_e \frac{\partial T_e}{\partial r}\right) + \sum_{\text{rays}} I_{\text{ray}} A_{\text{ray}} \times [1 - \exp(-\alpha s)] - 3k_b(T_e - T_g)n_e m_e \sum_{\text{heavies}}\left(\frac{\bar{\nu}_{es}}{m_s}\right) - \sum_{\text{bands}} (4\pi)(5.44 \times 10^{-52})G_{ff}\left[\frac{n_e(n_a + n_i)}{\sqrt{T_e}}\right] \times \exp\left[\frac{4(a_0^3 n_e)^{4/15}Ry - h\nu}{(k_b T_e/jev)}\right]\exp\left[\frac{-\Delta E_\infty}{(k_b T_e/jev)}\right] \quad (1)$$

in which the first summation represents power absorbed from the incident beam, the second summation represents elastic collisional energy transfer between the electrons and the heavy species, and the third summation represents optically thin radiation loss that was computed as a summation of electron-ion and electron-atom bremsstrahlung radiation over frequency bands.[1,21]

The computation of the beam absorption involves computation of the total absorption coefficient α, coupled with an algorithm for tracing individual rays through a spherical focusing lens and then through the computational domain, in which the index of refraction was a function of local conditions. A detailed description of the ray trace algorithm, which tracked and attenuated 25 rays, may be found in Ref. 1 and will not be presented here due to space considerations.

The incident beam was assumed to be annular with a 50 mm i.d. and a 75 mm o.d. to match the measured approximate beam size of the UIUC 10-kW CO_2 laser.[2] Attenuation of the beam was computed through Beer's law as indicated in the electron energy equation. The total absorption coefficient was computed from the sum of electron-ion, electron-neutral atom, and electron-molecular IB absorption coefficients.[1]

The source term for elastic collisional energy transfer[22-24] in the electron energy equation was a summation of electron collisions with the heavy species in which m_e is the electron mass, m_s is the heavy particle mass, and $\bar{\nu}_{es}$ is the average collision frequency between electrons and each heavy species. The average collision frequency is given by

$$\bar{\nu}_{es} = \bar{C}_e n_s Q_{es} \quad (2)$$

in which Q_{es} is the collision cross section between electrons and species s, n_s is the number density of species s, and $\bar{C}_e$ is the mean thermal speed of the electrons given by

$$\bar{C}_e = \sqrt{(8k_b T_e/\pi m_e)} \quad (3)$$

The collision cross sections required for the elastic transfer computation may be divided into three categories: 1) Coulomb, 2) electron-atom, and 3) electron-H_2 collisions. The collision cross sections for electron-atom and electron-H_2 collisions were computed from the tabulations of Itikawa.[25,26] The cross section for Coulomb collisions may be written[27]

$$Q_{ei} = \frac{\pi e^4 k_c^2 (/\!/\, \Lambda_e)}{2(k_b T_e)^2} \quad (4)$$

in which k_c is the Coulomb constant (necessary for proper conversion to mks units), and Λ_e is the Spitzer logarithm given by

$$\Lambda_e = \left[\frac{1.5\sqrt{(k_b^3 T_e^3/\pi n_e)}}{e^3 k_c^{1.5}}\right] \quad (5)$$

The model heavy energy equation is

$$\frac{\partial}{\partial x}\left[\left(\frac{3}{2}n_h k_b u\right)T_g\right] + \frac{1}{r}\frac{\partial}{\partial r}\left[\left(\frac{3}{2}rn_h k_b v\right)T_g\right] = \frac{\partial}{\partial x}\left(\lambda_h \frac{\partial T_g}{\partial x}\right) + \frac{1}{r}\frac{\partial}{\partial r}\left(r\lambda_h \frac{\partial T_g}{\partial r}\right) - (P + p)\left[\frac{\partial u}{\partial x} + \frac{1}{r}\frac{\partial}{\partial r}(rv)\right] + 3k_b(T_e - T_g)n_e m_e \sum_{\text{heavies}}\left(\frac{\bar{\nu}_{es}}{m_s}\right) \quad (6)$$

where the last two terms represent the flow work and elastic collisional transfer.

The boundary conditions for both energy equations are fixed temperatures at the domain inlet, zero radial derivatives at the axis of symmetry and the outer wall, and zero axial derivative at the domain exit plane.

The axisymmetric axial momentum equation for variable density and viscosity is

$$\frac{\partial}{\partial x}(\rho uu) + \frac{1}{r}\frac{\partial}{\partial r}(r\rho uv) = \frac{4}{3}\frac{\partial}{\partial x}\left(\mu\frac{\partial u}{\partial x}\right) + \frac{1}{r}\frac{\partial}{\partial r}\left(\mu r\frac{\partial u}{\partial r}\right) - \frac{2}{3}\frac{\partial}{\partial x}\left(\mu\frac{\partial v}{\partial r}\right) - \frac{2}{3r}\frac{\partial}{\partial x}(\mu v) + \frac{1}{r}\frac{\partial}{\partial r}\left(\mu r\frac{\partial v}{\partial x}\right) - \frac{\partial p}{\partial x} - \rho g \quad (7)$$

where the last term is the gravity body force in the negative x direction. The boundary conditions for the axial momentum equation are fixed axial velocity at the domain inlet, zero velocity at the wall, zero radial derivative at the axis of symmetry, and zero axial gradient at the domain exit plane.

The axisymmetric radial momentum equation for variable density and viscosity is

$$\frac{\partial}{\partial x}(\rho uv) + \frac{1\partial}{r\partial r}(r\rho vv) = \frac{\partial}{\partial x}\left(\mu\frac{\partial v}{\partial x}\right) + \frac{4}{3r}\frac{\partial}{\partial r}\left(\mu r\frac{\partial v}{\partial r}\right) + \frac{\partial}{\partial x}\left(\mu\frac{\partial u}{\partial r}\right) - \frac{2}{3r}\frac{\partial}{\partial r}\left(\mu r\frac{\partial u}{\partial x}\right) + \frac{2\mu}{3r}\frac{\partial u}{\partial x} - \frac{\partial p}{\partial r} - \frac{4}{3}\frac{\mu v}{r^2} - \frac{2v}{3r}\frac{\partial \mu}{\partial r} \quad (8)$$

The boundary conditions for the radial momentum equation are zero radial velocity at the domain inlet, the axis of symmetry and the outer wall, and zero axial gradient at the domain exit plane.

The bulk continuity equation for a variable density axisymmetric cylindrical system is

$$\frac{\partial}{\partial x}(\rho u) + \frac{1\partial}{r\partial r}(r\rho v) = 0 \quad (9)$$

which is used in the SIMPLE algorithm to solve for variation in the local pressure p.[28]

The computation of the major species number density requires four equations for the four unknowns. The first of these equations represents charge neutrality and is referred to as the condition of quasineutrality given by

$$n_e = n_{H^+} \quad (10)$$

The second equation required to compute the number densities is the equation of state[29]

$$P = (n_e k_b T_e + n_h k_b T_g)(1 - P_c^{DH}) \quad (11)$$

where P is the system pressure, and P_c^{DH} is the Debye-Hückel pressure correction which, neglecting the minor species, is[29]

$$P_c^{DH} = \frac{\left[\frac{4\pi e^2 k_c}{k_b}\left(\frac{n_e}{T_e} + \frac{n_{H^+}}{T_g}\right)\right]^{1.5}}{24\pi(n_e + n_h)} \quad (12)$$

The last two equations required to compute the number densities are the dissociation and ionization laws of mass action, which are respectively given by[1]

$$\frac{(n_H)^2}{n_{H_2}} = \exp\left(\frac{-E_{H_2 d}}{k_b T_g}\right)\left(\frac{\pi m_H k_b T_g}{h^2}\right)^{3/2}\left[\frac{(Z_{Hex})(2T_e/T_g)}{(Z_{H_2 rot})(Z_{H_2 vib})}\right] \quad (13)$$

$$n_e\left(\frac{n_{H^+}}{n_H}\right)^{(T_g/T_e)} = \left[\frac{2\exp\left(\frac{-E_i}{k_b T_e}\right)\left(\frac{2\pi m_e k_b T_e}{h^2}\right)^{3/2}}{Z_{Hex}}\right] \quad (14)$$

in which the E terms in the exponents represent zero point energies, and the Z terms represent partition functions. The derivations of Eqs. (13) and (14) began with a form of the law of mass action as used by Eddy and Cho,[30] which is based on minimization of Gibbs free energy. More recently, Martinez-Sanchez has rederived the law of mass action based on maximization of entropy. Apparently in multitemperature systems, the equilibrium state is given by the state of maximum entropy, but not by the minimum Gibbs free energy.[31] The difference turns out to be that the ratios of temperatures appearing in the exponents of Eqs. (13) and (14) are removed, and replaced by unity. Morro and Romeo[32] have also derived a law of mass action for multitemperature systems in which the temperature ratios have been replaced by unity.

It has not been determined whether or not the temperature ratios have a significant effect on the number density computations in this work. However, it can be pointed out that in experimental work involving argon LSPs, errors introduced by retaining the temperature ratios are not significant.[33] In addition, since the results of this work show no significant kinetic nonequilibrium except in regions outside of the LSP core, the question of the temperature ratios may be moot.

Transport coefficients used in the conservation equations were to be computed using high levels of approximation of the Chapman-Enskog technique as appropriate for cases for which there is a high degree of ionization.[34] Unfortunately, all the necessary collision integrals required for this computation could not be reliably located. Therefore a compromise was made with regard to the transport coefficients, and very simplified expressions were used.

Electron thermal conductivity was approximated by an algebraic expression, and the heavy species thermal conductivity and viscosity have been curve fit against temperature and pressure using LTE data from Kovitya[35] and Cebeci and Bradshaw.[36] The data taken from Kovitya[34] is valid from 5000 to 60,000 K gas temperature, and for pressures from 1 to 100 atm. The data taken from Cebeci and Bradshaw[36] is valid for 1 atm and gas temperatures from 300 to 1300 K. Curve fits were constructed from 300 to 60,000 K gas temperature, and pressures of 1, 10, and 100 atm for viscosity and heavy species thermal conductivity. Values for the model were then interpolated between the curve fits as necessary.

Electron thermal conductivity was based approximately on the values used by Chen[37] for electron thermal conductivity in an argon plasma, and is given by the expression

$$\lambda_e = 5 \times 10^{-25} n_e \sqrt{T_e} \quad (15)$$

Numerical Solution Method

The solution algorithm for the kinetic nonequilibrium model was iterative involving repeated looping through the conser-

vation and species number density equations, and using the SIMPLE algorithm of Patankar.[28] The SIMPLE algorithm is an iterative pressure-based Navier-Stokes solver that solves the continuity equation as a pressure correction equation. The power law discretization scheme was applied in which the order of accuracy is dependent upon the value of the cell face Peclet number. For absolute values of Peclet number greater than 10, the scheme reduces to an upwind scheme (purely convective), which is first-order accurate. For absolute values of Peclet number less than 10, the scheme includes diffusion and is second-order accurate.

Five different computational domains were used in this work depending upon the parameters for the focusing lens and the domain length. A summary of domains appears in Table 2. Each of the domains had the same grid cell dimensions in the region of the beam focus (first third of the domain axially and first half of the domain radially). Solutions were invariant to domain length as can be seen by comparison of the results of cases 23 and 26 that show negligible differences.

Following the selection of the desired grid and optical parameters, the model LSP was initiated and allowed to relax to a steady-state solution. Experimentally, initiation was accomplished by inserting a tungsten rod into the beam focus. The rod released free electrons that immediately began absorbing the incident laser beam and subsequently caused a plasma breakdown through continuous heating and collisions with heavy species. Although it qualitatively represents a point input of power at the beam focus, this phenomenon is not well described spatially or in the amount of energy initially distributed in the electrons ejected by the tungsten rod. Therefore, there is no definitive method in which the model plasma could be started that would exactly match experimental conditions.

Table 2 Computational domains

Domain	Grid	Size, mm	f-Number
D	100 × 50	304.8 × 63.5	4
F	100 × 50	304.8 × 63.5	8
G	100 × 50	304.8 × 63.5	2
H	100 × 50	406.4 × 63.5	4
L	100 × 50	812.8 × 63.5	4

A typical model run was started assuming an unheated flow of gas through the chamber and an unperturbed incident beam. A small amount of energy was deposited near the focus of the unperturbed beam, which was known based upon the beam ray trace. The result was a spike in electron temperature that then gradually relaxed as plasma breakdown was simulated numerically by the species computation. This method of initiation was labeled as the point spark method. Alternately, other methods could be used to spark the LSP depending upon the initial distribution and magnitude of sparks employed, or the temperature field of a previous case could be used.

Each test case was considered to be converged when the normalized residual for each of the conservation equations was driven below the convergence criterion, typically set to be 10^{-4} for the energy equations and 10^{-5} for the momentum and continuity equations. The energy residuals were normalized by the input beam power, the momentum residuals were normalized by the momentum flux at the inlet, and the continuity residual was normalized by the mass flow into the domain.

Model Results

Simplified model results for global absorption and thermal efficiency are presented and compared with experimental results. Contour plots of selected quantities are also presented to illustrate physical phenomena and make case comparisons. The two global figures of merit may be computed from the solution fields. Global absorption α may be written as

$$\alpha = \frac{\sum_{\text{domain}} (2\pi)\ (\text{power absorbed})}{\text{beam power}} \tag{16}$$

Thermal efficiency η may be written as

$$\eta = \frac{\dot{m}(h_{\text{exit}} - h_{\text{inlet}})}{\text{beam power}} \tag{17}$$

Table 3 Global results of test cases

Case	Domain	Power, kW	Pressure, atm	Mole flux	abs, %	eff, %	Peak T_e, K	Peak T_g, K	Ratio of peak temperatures
1	D	70	3.5	2,192.9	99.38	32.64	40,068	39,993	1.002
2	D	70	7	2,192.9	99.93	23.77	44,870	44,823	1.001
3	D	3.5	3.5	1,507.6	82.93	73.19	17,352	17,349	1.000
4	D	3.5	3.5	1,781.8	85.30	74.56	22,237	22,227	1.000
5	D	7	3.5	1,644.7	94.09	72.80	21,146	21,142	1.000
6	D	7	3.5	2,192.9	94.38	79.72	20,439	20,434	1.000
7	H	700	3.5	2,192.9	99.95	13.19	69,522	67,980	1.023
8	H	70	1	2,192.9	89.63	58.65	29,184	29,084	1.003
9	F	7	3.5	2,192.9	94.50	75.27	24,158	24,150	1.000
10	G	7	3.5	2,192.9	94.36	76.48	21,498	21,490	1.000
11	D	7	3.5	1,918.8	94.30	75.71	20,725	20,720	1.000
12	D	3.5	3.5	2,192.9	85.48	76.14	21,606	21,596	1.000
13	D	3.5	3.5	1,644.7	84.83	73.69	22,318	22,309	1.000
14	D	3.5	3.5	2,467.1	85.06	77.33	21,081	21,071	1.000
15	D	3.5	3.5	3,015.3	83.79	81.25	19,666	19,655	1.001
16	H	70	0.5	1,096.5	64.77	53.62	24,163	24,003	1.005
17	H	700	0.5	1,096.5	92.53	57.56	41,595	39,418	1.055
18	H	70	0.25	1,096.5	17.25	16.80	18,812	18,565	1.013
19	H	700	0.25	1,096.5	65.39	59.16	32,577	30,552	1.066
20	H	70	3.5	4,385.8	99.65	42.30	39,181	39,112	1.002
21	H	70	3.5	5,482.3	99.75	44.86	40,084	40,007	1.002
22	H	70	7	8,223.4	99.995	42.87	42,834	42,799	1.001
23	H	700	1	2,192.9	98.82	35.63	49,822	47,721	1.044
24	H	700	2	2,192.9	99.65	19.50	60,868	58,811	1.035
25	H	700	2	2,741.1	99.56	21.55	61,210	59,176	1.034
26	L	700	1	2,192.9	98.50	35.61	49,394	47,330	1.044
27	L	700	1	3,289.4	98.90	40.49	48,775	46,772	1.043

It was found that multiple initial condition dependent solutions could be produced, however, due to space considerations this effect will not be discussed in detail in this article. A listing of model results using point spark initiation appears in Table 3.

Comparison with Experiments

Despite the fact that the model has demonstrated multiple solutions dependent upon initial conditions, comparisons can still be made with the experimental results in terms of performance and stability. Model results generated with a point spark will be used for comparison purposes since the point spark most closely resembles experimental LSP initiation. Model predictions for global absorption and thermal efficiency for a series of 7 kW, f-4, 3.5 atm LSPs can be seen

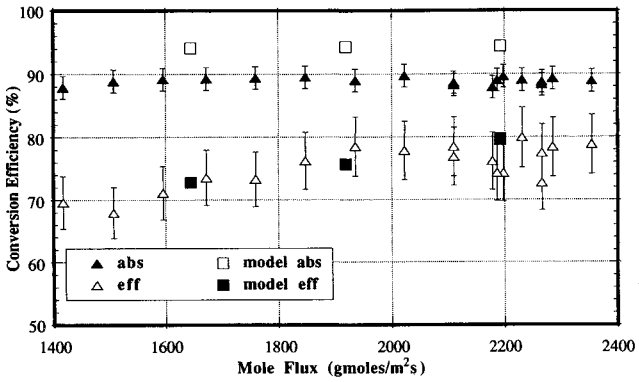

Fig. 1 Comparison of model predictions for global absorption and thermal efficiency of 7 kW, f-4, 3.5 atm hydrogen LSPs and experimentally determined global absorption and thermal efficiency of 7 kW, f-4.1, hydrogen LSPs at 3.52 ± 0.10 atm[3].

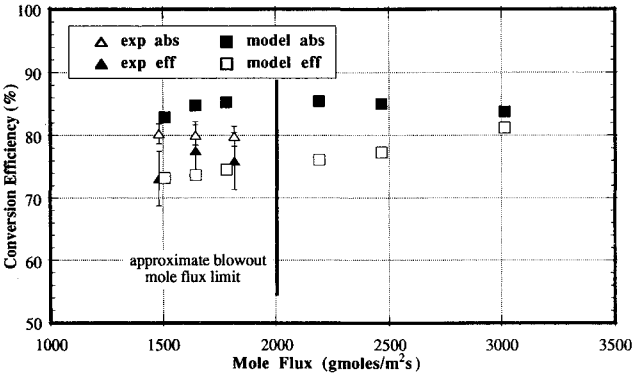

Fig. 2 Comparison of model predictions for global absorption and thermal efficiency of 3.5 kW, f-4, 3.5 atm hydrogen LSPs and experimentally determined global absorption and thermal efficiency of 3.5 kW, f-4.1, hydrogen LSPs at 3.56 ± 0.02 atm[3].

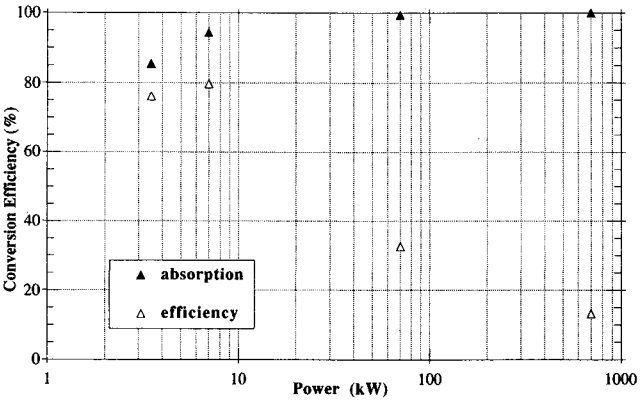

Fig. 3 Model results for global absorption and thermal efficiency vs incident power for 3.5 atm, f-4, 2192 mole/m²s hydrogen LSPs.

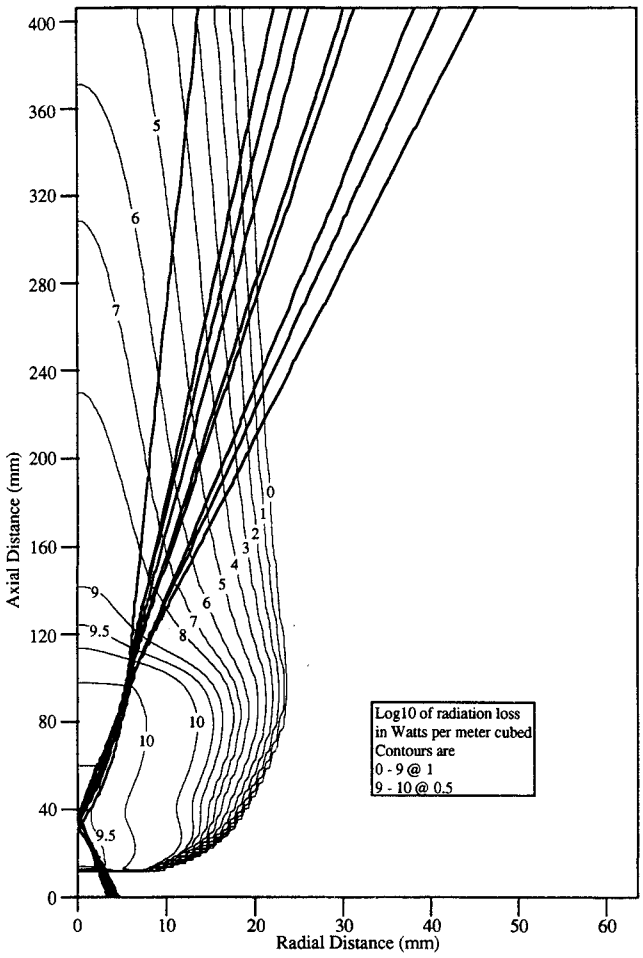

Fig. 4 Contours of the base 10 log of radiation loss in W/m³ from case 7 (700 kW).

compared with experimental results for similar conditions in Fig. 1.

Based upon the data in Fig. 1, it would appear that at 7 kW, f-4, and 3.5 atm, the model slightly overpredicts global absorption. However, it is also possible that the experimental global absorption data had a systematic error associated with it which caused the measurements to come out low. This error could have been due to plasma irradiation of the calorimeter cone on top of the absorption chamber that had been assumed to be negligible as described in Ref. 2. The essentially constant model global absorption with increased mole flux agrees well with experimental results.

Model predictions for thermal efficiency at 7 kW, f-4, 3.5 atm appear to match experimental values both in magnitude and trend. No comparison can be made for blowout predictions at these conditions, however, because none of the 7 kW, 3.5 atm, f-4.1 experimental LSPs were blown out. Overall it would appear that there is fair agreement between model predictions and experimental results at 7 kW, f-4, and 3.5 atm.

Model predictions for global absorption and thermal efficiency for a series of 3.5 kW, f-4, 3.5 atm LSPs can be seen compared with experimental results for similar conditions in Fig. 2. The experimental 3.5 kW LSPs did demonstrate a blowout as marked on the plot in Fig. 2. Note that once again the model slightly overpredicts global absorption compared with experimental values. The model results also indicate a slight variation in global absorption with increasing mole flux, but this effect is minor.

Thermal efficiency as predicted by the model compares very well with the experimental results. However, a large discrepancy is visible in Fig. 2 between the experimentally determined blowout mole flux and the model blowout mole flux.

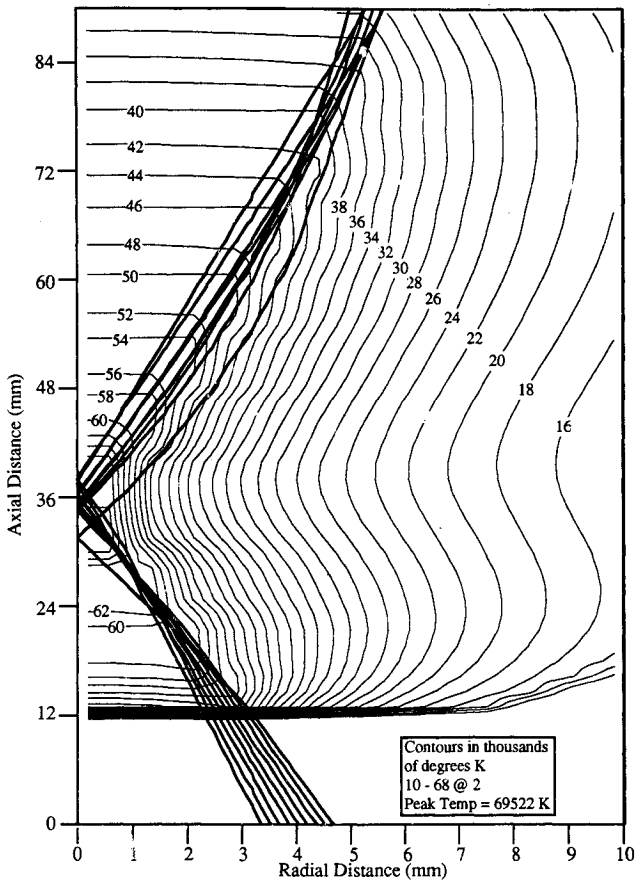

Fig. 5 Electron temperature contours of the core region of case 7 (700 kW).

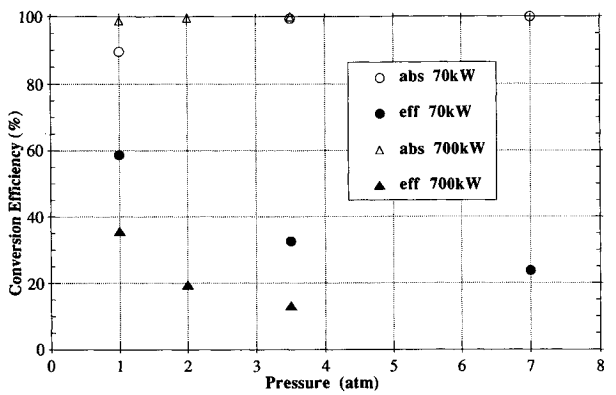

Fig. 6 Model predictions for global absorption and thermal efficiency for 70 and 700 kW hydrogen LSPs vs pressure.

It should be realized that experimentally, as LSPs approach the blowout limit, any small perturbations in the operating parameters can cause the plasma to prematurely extinguish. This is the major reason why blowout mole fluxes are difficult to exactly determine.

In addition, it has been observed experimentally as documented by Zerkle[38] that the symmetry of the incident annular beam has an effect on the blowout mole flux. It is possible that since the model assumes a symmetrical beam that predictions for blowout mole flux would therefore be higher than what was observed experimentally due to laboratory beam asymmetries.

Theoretically, the blowout mole flux is reached when the value for thermal efficiency closely approaches the value for global absorption, representing a negligible radiation loss. Because there are no random perturbations in the model, a blowout prediction would be expected to correspond to the case where the values for global absorption and thermal efficiency come together. If one were to extrapolate the model data, this would occur at a mole flux near 3400 moles/m^{2}s. Therefore, the model does only a fair job of predicting blowout mole flux, however, this may be due to nonideal factors that are not even included in the model, such as beam asymmetries or experimental perturbation of control parameters.

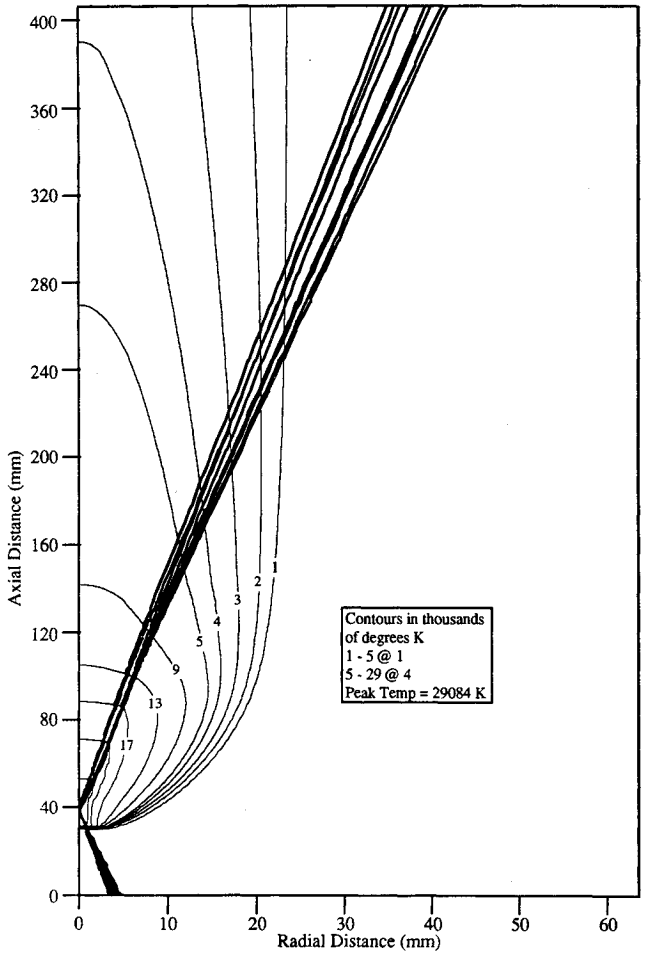

Fig. 7 Heavy species temperature contours for case 8 (70 kW, 1 atm).

Effect of Control Parameters

The variation of predicted global performance vs changes in mole flux have already been demonstrated in the plots of Figs. 1 and 2. Model global absorption is essentially constant vs mole flux, however, model thermal efficiency increases with mole flux. Both these trends agree well with experimental results.[3] In addition, a closer examination of LSP temperature and radiation fields reveals that an increase in mole flux causes the LSP to slightly increase in length, and decrease in peak temperature.

Model predictions for global absorption and thermal efficiency for cases at f-4, 3.5 atm, and 2192.9 moles/m^{2}s have been plotted against incident power in Fig. 3. Predicted global absorption follows the experimentally observed trend of increasing with laser power,[3] appearing to asymptote to 100%. For a fixed mole flux, thermal efficiency decreases with increased incident power, due to an increased fraction of the absorbed power lost as radiation from the LSP. In the figures that follow, the darker lines starting at the domain inlet and reflecting at (passing through) the axis, represent the path of the incident beam as represented by a ray-trace using 9 rays. Both the direction of beam travel and gas flow are bottom to top, and the left side of the domains represent an axis of symmetry.

There is a tremendous increase in radiating volume with incident power, and the region of maximum radiation loss

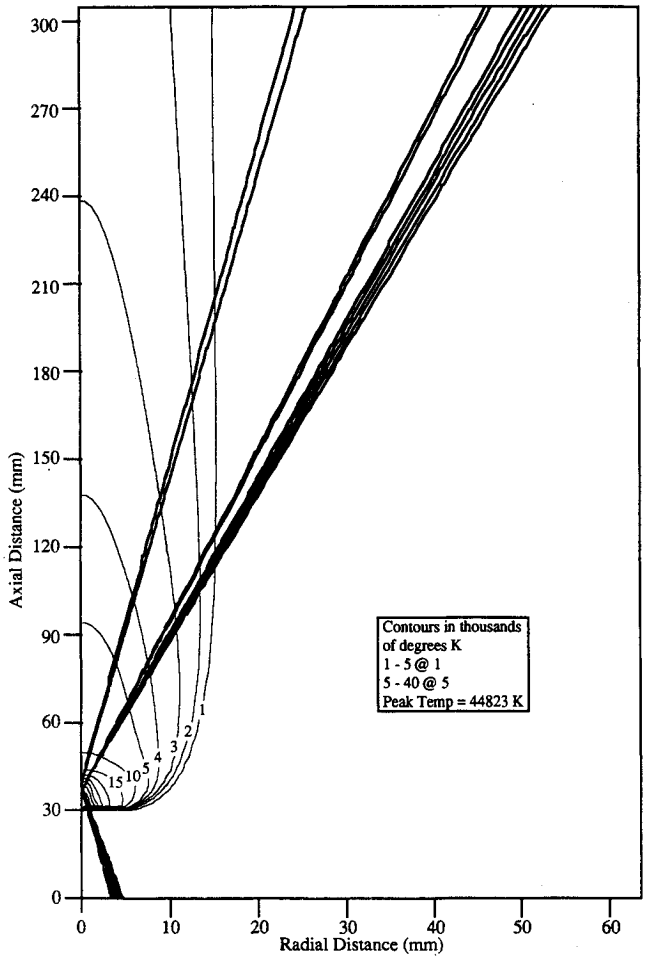

Fig. 8 Heavy species temperature contours for case 2 (70 kW, 7 atm).

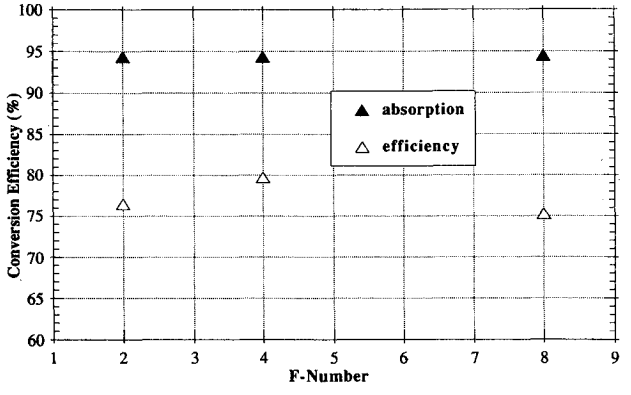

Fig. 9 Model predictions for global absorption and thermal efficiency for 3.5 atm, 7 kW, 2192.9 mole/m²s hydrogen LSPs vs beam f-number.

moves farther from the axis as power is increased. This maximum radiation loss region corresponds to an electron temperature between 16,000 and 17,000 K at 3.5 atm, and can clearly be seen in the plot of radiation loss contours for case 7 in Fig. 4. This temperature region moves away from the axis with increased power, because of increased peak electron temperatures on the axis. There is a dramatic peak electron temperature increase between 7 (20,439), 70 (40,068), and 700 kW (69,522 K). Electron temperature contours for the core region of case 7 can be seen in the plot of Fig. 5.

The final comparison to be made with power variation is the location of maximum beam absorption. As power is increased and peak temperature rises, the absorption coefficient along the path of the beam is decreased. The vast majority of power is absorbed at or near the focus in the 7-kW case.

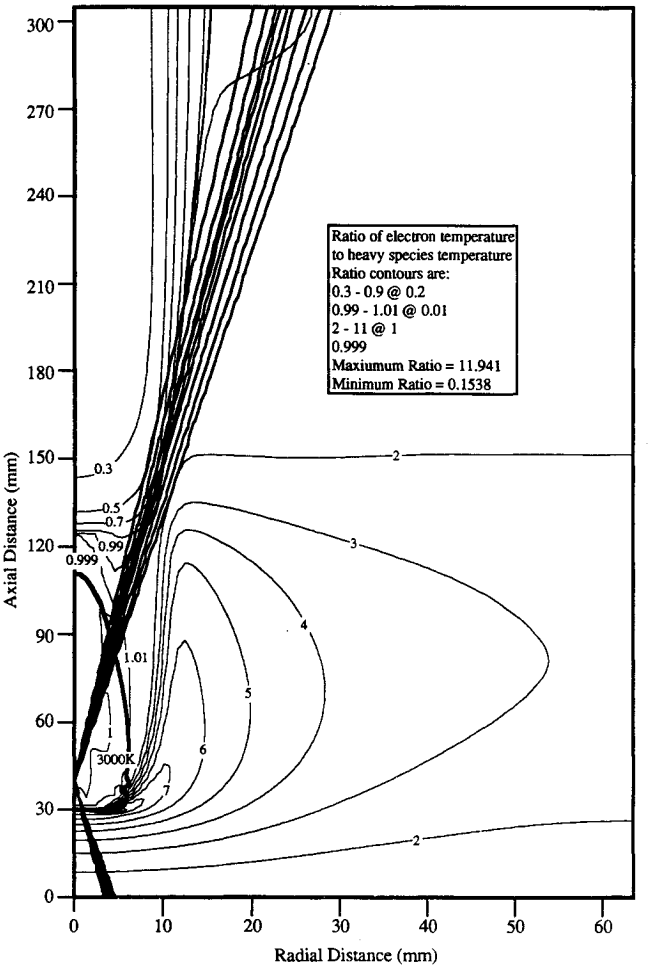

Fig. 10 Contours of the ratio of electron temperature to heavy species temperature for case 6.

However, absorption of the beam is far more gradual for the 700-kW case, with the region of maximum absorption actually occurring just downstream of the laser focus on the axis of symmetry.

Model results for global absorption and thermal efficiency for 70 and 700 kW, 2192.9 moles/m²s, f-4 hydrogen LSPs can be seen in the plot of Fig. 6. Predicted global absorption follows the experimentally observed trend of increasing with increased pressure,[3] appearing to asymptote to 100%. For a fixed mole flux, thermal efficiency decreases with increased gas pressure due to a larger fraction of the absorbed power lost as radiation. It is clear from the heavy species temperature contour plots appearing in Figs. 7 and 8 for cases 8 and 2, respectively, that an increase in gas pressure results in a decrease in both LSP length and width.

In addition to a decrease in size, a peak temperature increase with increased pressure was observed. Peak heavy species temperatures for the 70-kW series were 29,084 K at 1 atm (case 8), 39,993 K at 3.5 atm (case 1), and 44,823 K at 7 atm (case 2).

Model results for global absorption and thermal efficiency for cases at 2192.9 moles/m²s, 7 kW, 3.5 atm, and three f-numbers can be seen in the plot of Fig. 9. Predicted global absorption is essentially constant vs f-number. Experimentally it was observed that global absorption slightly decreased when f-number was increased from f-4.1 to f-7.1.[3]

Referring to the data in Fig. 9, thermal efficiency increases between f-2 and f-4, but decreases between f-4 and f-8. The location of the peak temperature in each case was just upstream of the beam focus in the direct path of the beam, and peak temperature was a maximum for the f-4 case.

Kinetic Nonequilibrium

The existence of kinetic nonequilibrium was thought to be a likely result of the model, especially at the test cases involving high power and low pressure. However, in regions of the plasma core, except for the cases at 700 kW, kinetic nonequilibrium was minimal. In fact, case 19 (700 kW, 0.25 atm), which was the case most likely to produce nonequilibrium results, had a maximum electron to heavy species temperature ratio of only 1.075 in the LSP core. For all cases, the electron and heavy species temperature contours for all temperatures greater than approximately 3000 K were almost completely identical. Below approximately 3000 K, however, there is a significant difference between electron temperature and heavy species gas temperature.

Starting with low power and high pressure, contours of the ratio of electron temperature to heavy species temperature for case 6 (7 kW, 3.5 atm) can be seen in the plot of Fig. 10. The 3000 K electron temperature contour has been included in the plot as reference. Note that there is a high degree of kinetic nonequilibrium just upstream and radially outward from the LSP front. Also note that in the LSP tail, beyond the 3000 K contour, the electron temperature drops below the heavy species temperature. However, for almost all of the region above 3000 K electron temperature, the value of the temperature ratio is very close to unity.

Examining a case of high power and high pressure, contours of the temperature ratio for case 7 (700 kW, 3.5 atm) are close to unity everywhere inside of the 3000 K electron temperature contour as can be seen in Fig. 11. Notice the 1.01 contour near the axis just downstream of the beam focus (actually the maximum core ratio is 1.023 for the ratio of peak temperatures). Again, kinetic nonequilibrium is evident for

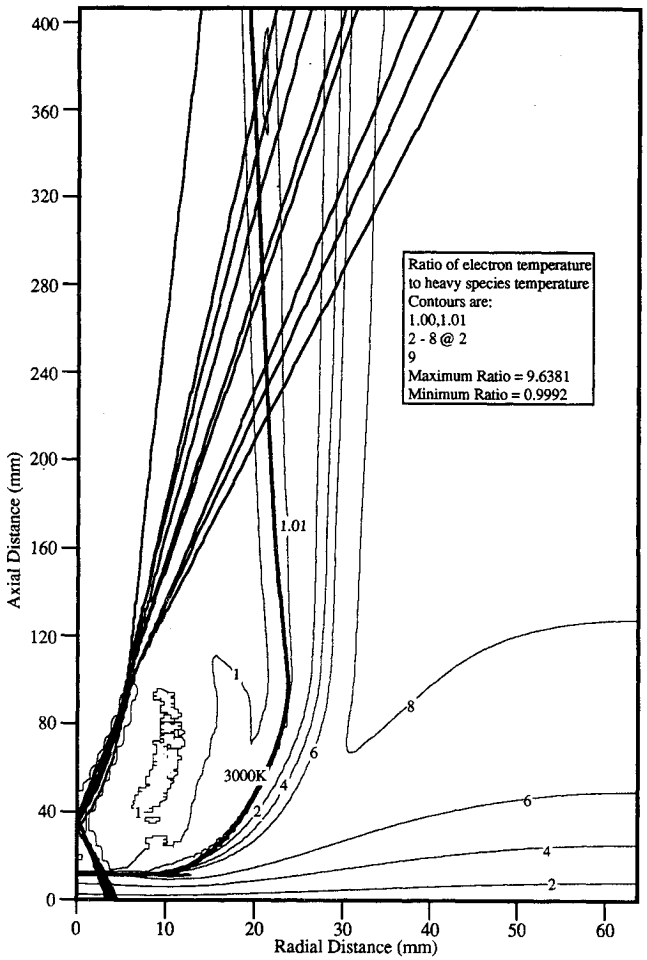

Fig. 11 Contours of the ratio of electron temperature to heavy species temperature for case 7.

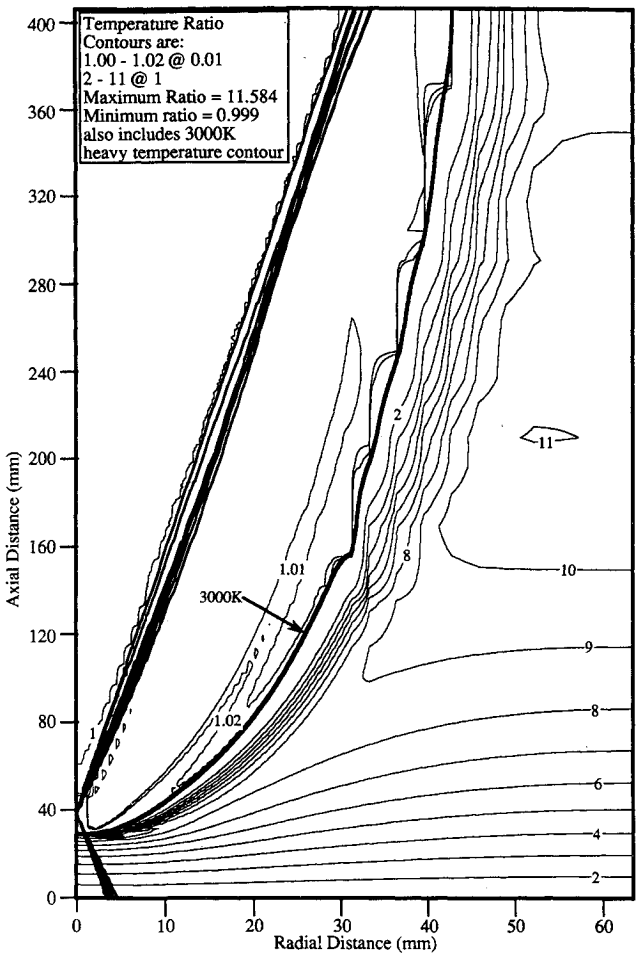

Fig. 12 Contours of the ratio of electron temperature to heavy species temperature for case 19.

the same region just upstream and radially outward from the plasma front. However, kinetic nonequilibrium is not evident in the tail of this case, because the temperatures are still sufficiently high. It is very interesting to note that the region of maximum kinetic nonequilibrium appearing just upstream and radially outward from the plasma front spatially corresponds exactly to the experimentally determined region of maximum kinetic nonequilibrium identified by Zerkle[20] for 7 kW argon LSPs.

Finally, examining a case with high power and low pressure, temperature ratio contours for case 19 (700 kW, 0.25 atm) have been plotted in Fig. 12. Note the region outside of the LSP core in which the temperature ratio once again greatly varies from unity. However, in the LSP core, kinetic nonequilibrium is not significant.

The reason for the lack of significant kinetic nonequilibrium for temperatures above approximately 3000 K is that the number density of electrons for the cases tested was sufficient to maintain equilibrium through elastic collisions. Below approximately 3000 K, the electron number density has decreased past the point where elastic collisional transfer is sufficient to maintain equilibrium. Therefore, in these regions, the electron temperature became uncoupled from the heavy species temperature.

In the region slightly upstream and radially outward from the plasma front, the uncoupled electron energy equation resembled a conduction equation, because the convective flux of electrons was negligible. Since the electrons were uncoupled from the heavy species and there was essentially no convection of cold electrons from upstream, heat was conducted outward toward the wall, which was assumed to be adiabatic, giving rise to kinetic nonequilibrium. In addition, there was

a tremendous flow expansion in the region of the plasma front that caused the heavy species temperature to cool through flow work.

Examination of the ratio contours in Figs. 10 and 11 reveals that the contour representing kinetic equilibrium (ratio = 1) does not form a closed path with the axis of symmetry in either plot. This is because in the regions downstream of the LSP core, where the electrons are no longer absorbing the beam, the temperature ratio is just less than unity. This behavior is due to the model assumption of optically thin radiation loss from the electrons. Therefore, the electrons in the core regions not in the path of the beam had a large radiative loss term, but a zero absorption term, which caused the electron temperature to be very slightly lower than the heavy species temperature.

An excellent example of this behavior can be seen in the plot of temperature ratio contours for case 7 appearing in Fig. 11. Referring to the island of roughly drawn contours approximately 10 mm from the axis, in the core, it can easily be determined that values within the island contour are less than unity. It is not surprising then to note that the position of the island corresponds exactly to the region of maximum radiation loss that can be seen in the plot of radiation loss contours for case 7 plotted in Fig. 4.

LSP Velocity Fields

The velocity fields of model LSPs exhibit similar qualitative features, regardless of the case conditions. The flowfields around the model LSPs were disturbed strongly in the vicinity of the plasma, near the core. The axial velocity upstream of the LSP typically slowed to a few meters per second or less, and then was greatly accelerated upon reaching the plasma front. There was some radial acceleration of the flow away from the axis, but the dominant effect was axial acceleration downstream accompanied by a dramatic decrease in gas density due to the extreme core temperatures. The extent of the acceleration and the size of the accelerated region depend upon the temperature and spatial extent of the plasma core. Diversion of mass around the LSP can clearly be seen in the plot of mass flow contours for case 7 in Fig. 13. This type of flow diversion in which the LSP acts as a semiporous bluff body to the mass flow was also noted by Eguiguren and Krier in their LTE argon LSP model.[19]

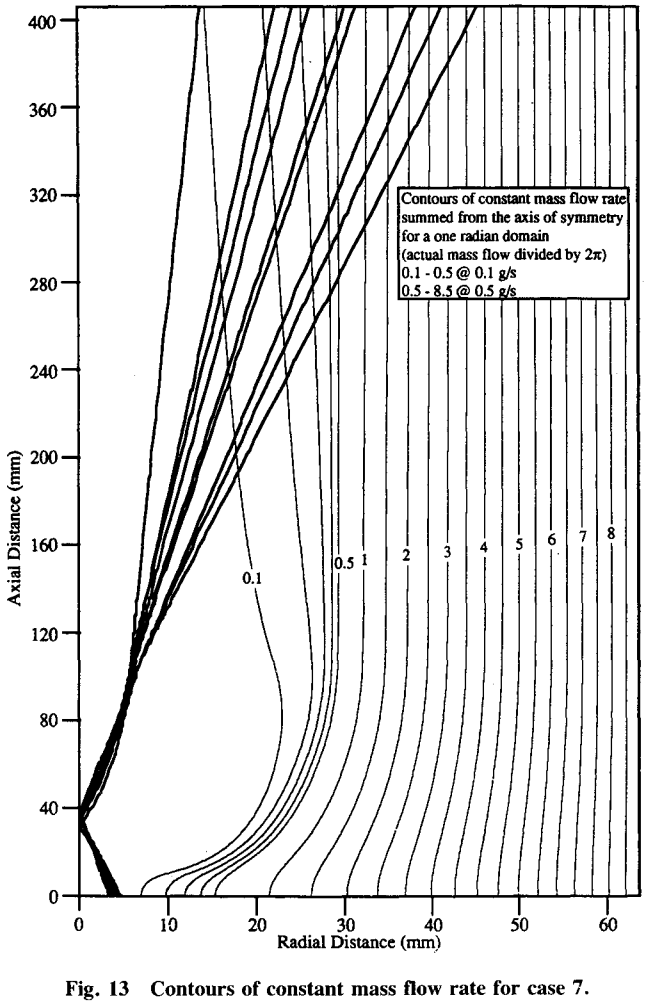

Fig. 13 Contours of constant mass flow rate for case 7.

Conclusions

Based upon the model results, the conclusions may be summarized as follows:

1) Model predictions for global absorption and thermal efficiency for point spark initiation followed experimental trends against variations in the control parameters well. In fact, the model data at 3.5 and 7 kW compared favorably with experimental data for similar conditions. Variations of model LSP size and shape vs variations of the control parameters also agreed well with experimental observations (photographic and visual).

The model prediction of blowout mole flux was high compared to the experimentally determined blowout mole flux at 3.5 kW, f-4.1, 3.5 atm. However, this may have been due to the idealized nature of the model with respect to beam symmetry and flow perturbations when compared with the actual experimental conditions as was previously described.

2) Refraction of the beam by the electrons in the plasma did not have a significant effect on plasma performance, except for cases that were initiated with something other than a point spark. The multiple solutions generated by different initial conditions were linked to beam refraction effects. The focusing effect on the incident beam caused by plasma refraction resulted in ring foci off the axis of symmetry for some cases.

3) Kinetic nonequilibrium was not significant in the region of the plasma core, or in fact anywhere in which the electron and heavy species temperatures were coupled through elastic collisions. In relatively cool outlying regions (below approximately 3000 K), there was significant kinetic nonequilibrium due to decoupling between the electrons and heavy species temperatures. However, because the electron number density was so low in these regions, kinetic nonequilibrium had little effect on LSP performance, as it would be expected to have if it existed significantly in the plasma core.

Acknowledgments

This research is supported by the Air Force Office of Scientific Research under Contract F49620-92-J-0448 (year 1); Mitat Birkan is Program Manager. The authors would like to thank Pratap Vanka of the Department of Mechanical and Industrial Engineering at the University of Illinois at Urbana-Champaign for our discussions relating to computational strategies and optimization of the solution technique.

References

[1]Krier, H., and Mertogul, A. E., "Two Temperature Modeling and Experimental Measurements of Laser Sustained Hydrogen Plasmas," Dept. of Mechanical and Industrial Engineering, Univ. of Illinois at Urbana-Champaign, Annual Technical Rept. UILU-ENG 93-4015, Urbana, IL, 1993.

[2]Zerkle, D. K., Schwartz, S., Mertogul, A. E., Chen, X., Krier, H., and Mazumder, J., "Laser-Sustained Argon Plasmas for Thermal Rocket Propulsion," *Journal of Propulsion and Power*, Vol. 6, No. 1, 1990, pp. 38–45.

[3]Mertogul, A., Zerkle, D., and Krier, H., "Investigation of CO_2 Laser-Sustained Hydrogen Plasmas," *Journal of Propulsion and Power*, Vol. 8, No. 5, 1992, pp. 1123–1125.

[4]Eskridge, R. H., McCay, T. D., and VanZandt, D. M., "An Experimental Study of Laser-Supported Plasmas for Laser Propulsion—Final Report," NASA George C. Marshall Space Flight Cen-

ter, NASA TM-86583, Jan. 1987.

[5]McCay, T. D., Eskridge, R. H., and VanZandt, D. H., "Experiments on Optical Discharges in Hydrogen," *Journal of Thermophysics and Heat Transfer*, Vol. 2, No. 4, 1988, pp. 317–323.

[6]VanZandt, D. M., McCay, T. D., and Eskridge, R. H., "An Experimental Study of Laser Supported Hydrogen Plasmas," AIAA Paper 84-1572, June 1984.

[7]Litvak, M. M., and Edwards, D. F., "Electron Recombination in Laser-Produced Hydrogen Plasma," *Journal of Applied Physics*, Vol. 37, No. 12, 1966, pp. 4462–4474.

[8]Kozlov, G. I., Kuznetsov, V. A., and Masyukov, V. A., "Sustained Optical Discharges in Molecular Gases," *Soviet Physics—Technical Physics* [*translation of Fizika Tverdogo Tela* (*Leningrad*)], Vol. 49, No. 11, 1979, pp. 1283–1287.

[9]Raizer, Y. P., "Subsonic Propagation of a Light Spark and Threshold Conditions for the Maintenance of Plasma by Radiation," *Soviet Physics JETP* (*translation of Zhurnal Eksperimental'noi i Teoretisch eskoi Fiziki*), Vol. 31, No. 6, 1970, pp. 1148–1154.

[10]Kemp, N. H., and Root, R. G., "Analytical Study of Laser-Supported Combustion Waves in Hydrogen," *Journal of Energy*, Vol. 3, No. 1, 1979, pp. 40–49.

[11]Muller, S., and Uhlenbusch, J., "Theoretical Model for a Continuous Optical Discharge," *Physica C*, Vol. 112, 1982, pp. 259–270.

[12]Molvik, G. A., Choi, D., and Merkle, C. L., "A Two-Dimensional Analysis of Laser Heat Addition in Converging Nozzles," AIAA Paper 84-0529, Jan. 1984.

[13]Merkle, C. L., Molvik, G. A., and Shaw, E. J.-H., "Numerical Solution of Strong Radiation Gasdynamic Interactions in a Hydrogen-Seedant Mixture," AIAA Paper 85-1554, July 1985.

[14]Glumb, R. J., and Krier, H., "Two-Dimensional Model of Laser-Sustained Plasmas in Axisymmetric Flowfields," *AIAA Journal*, Vol. 24, No. 8, 1986, p. 1331–1336.

[15]Jeng, S. M., and Keefer, D. R., "Numerical Study of Laser-Sustained Hydrogen Plasmas in a Forced Convective Flow," *Journal of Propulsion and Power*, Vol. 3, No. 3, 1987, pp. 255–261.

[16]Jeng, S. M., and Keefer, D. R., "A Theoretical Investigation of Laser-Sustained Plasma Thruster," AIAA Paper 87-0383, Jan. 1987.

[17]Beddini, R. A., Owano, T. G., and Kuo, S.-L., "Analysis of Gas Dynamic Interactions with Intense Optical Beams," AIAA Paper 87-1455, June 1987.

[18]Beddini, R. A., and Owano, T. G., "Analysis of Turbulent Convective and Radiative Heat Transfer in High Temperature Rocket Chamber Flows," AIAA Paper 87-1770, July 1987.

[19]Eguiguren, J. V., and Krier, H., "Laser-Sustained Plasmas in a Forced Convective Flow," Dept. of Mechanical and Industrial Engineering, Univ. of Illinois at Urbana-Champaign, Annual Technical Rept. UILU-ENG 89-4011, Urbana, IL, 1989.

[20]Zerkle, D. K., "Non-Local Thermodynamic Equilibrium in Laser Sustained Plasmas," Ph.D. Dissertation, Dept. of Mechanical and Industrial Engineering, Univ. of Illinois at Urbana-Champaign, Urbana, IL, Oct. 1992.

[21]Eddy, T. L., Leger, J. M., Coudert, J. F., and Fauchais, P., "Nonequilibrium Diagnostics of a Nitrogen Plasma Jet," *Heat Transfer in Thermal Plasma Processing*, American Society of Mechanical Engineers, HTD-Vol. 161, 1991, pp. 67–77.

[22]Chen, D. M., and Pfender, E., "Two-Temperature Modeling of the Anode Contraction Region of High-Intensity Arcs," *IEEE Transactions on Plasma Science*, Vol. PS-9, No. 4, 1981, pp. 265–274.

[23]Kruger, C. H., "Nonequilibrium in Confined-Arc Plasmas," *Physics of Fluids*, Vol. 13, No. 7, 1970, pp. 1737–1746.

[24]Kruger, C. H., and Mitchner, M., "Kinetic Theory of Two Temperature Plasmas," *Physics of Fluids*, Vol. 10, No. 9, 1967, pp. 1953–1961.

[25]Itikawa, Y., "Momentum-Transfer Cross Sections for Electron Collisions with Atoms and Molecules," *Atomic Data and Nuclear Data Tables*, Vol. 14, No. 1, 1974, pp. 1–10.

[26]Itikawa, Y., "Momentum-Transfer Cross Sections for Electron Collisions with Atoms and Molecules, Revision and Supplement," *Atomic Data and Nuclear Data Tables*, Vol. 21, No. 1, 1978, pp. 69–75.

[27]Jaffrin, M. Y., "Shock Structure in a Partially Ionized Gas," *Physics of Fluids*, Vol. 8, No. 4, 1965, pp. 606–625.

[28]Patankar, S. V., *Numerical Heat Transfer and Fluid Flow*, Hemisphere, New York, 1980.

[29]Cho, K. Y., "Nonequilibrium Thermodynamic Models and Applications to Hydrogen Plasma," Ph.D. Dissertation, Georgia Inst. of Technology, Atlanta, GA, 1988.

[30]Eddy, T. L., and Cho, K. Y., "A Multitemperature Model for Plasmas in Chemical Nonequilibrium," *Heat Transfer in Thermal Plasma Processing*, American Society of Mechanical Engineers, HTD-Vol. 161, 1991, pp. 195–210.

[31]Martinez-Sanchez, M., private communication, Massachusetts Inst. of Technology, Dept. of Aeronautics and Astronautics, Cambridge, MA, June 1993.

[32]Morro, A., and Romeo, M., "The Law of Mass Action for Fluid Mixtures with Several Temperatures and Velocities," *Journal of Non-Equilibrium Thermodynamics*, Vol. 13, No. 4, 1988, pp. 339–353.

[33]Zerkle, D. K., private communication, Los Alamos National Lab., Los Alamos, NM, June 1993; also Zerkle, D. K., and Krier, H., "Nonlocal Thermodynamic Equilibrium in Laser Sustained Plasmas," *AIAA Journal*, Vol. 32, No. 2, 1994, pp. 324–332.

[34]Devoto, R. S., "Transport Properties of Ionized Monatomic Gases," *Physics of Fluids*, Vol. 9, No. 6, 1966, pp. 1230–1240.

[35]Kovitya, P., "Physical Properties of High-Pressure Plasmas of Hydrogen and Copper in the Temperature Range 5000–60,000 K," *IEEE Transactions on Plasma Science*, Vol. PS-13, No. 6, 1985, pp. 587–594.

[36]Cebeci, T., and Bradshaw, P., *Physical and Computational Aspects of Convective Heat Transfer*, Springer-Verlag, New York, 1984.

[37]Chen, D. M., "Analytical Modeling of Two-Temperature Argon Arc Plasmas," Ph.D. Dissertation, Univ. of Minnesota, Minneapolis, MN, 1980.

[38]Zerkle, D. K., "Energy Conversion Measurements in Laser-Sustained Argon Plasmas at Elevated Mass Flux and Pressure," M.S. Thesis, Dept. of Mechanical and Industrial Engineering, Univ. of Illinois at Urbana-Champaign, Urbana, IL, May 1988.